Wearable cardiorespiratory monitoring with stretchable elastomer optical fiber

BINGJIE ZHA,[1] ZHUO WANG,[1] LINQING LI,[1] XUEHAO HU,[2] (iD) BEATRIZ ORTEGA,[3] XIAOLI LI,[1] AND RUI MIN[1,*]

[1]*Center for Cognition and Neuroergonomics, State Key Laboratory of Cognitive Neuroscience and Learning, Beijing Normal University, Zhuhai 519087, China*
[2]*Department of Electromagnetism and Telecommunication, University of Mons, Boulevard Dolez 31, 7000 Mons, Belgium*
[3]*ITEAM Research Institute, Universitat Politécnica de Valéncia, 46022 Valencia, Spain*
rumi@doctor.upv.es

Abstract: This work presents a stretchable elastomer optical fiber sensor incorporated into a belt for respiratory rate (RR) and heart rate (HR) monitoring. Different materials and shapes of prototypes designed were tested in terms of performance and the best choice was identified. The optimal sensor was tested by 10 volunteers to evaluate the performance. The proposed elastomer optical fiber sensor can achieve simultaneous measurement of RR and HR in different body positions, and also ballistocardiography (BCG) signal measurement in the lying position. The sensor has good accuracy and stability, with maximum errors of 1 bpm and 3 bpm for RR and HR, respectively, and average weighted mean absolute percentage error (MAPE) of 5.25% and root mean square error (RMSE) of 1.28 bpm. Moreover, the results of the Bland-Altman method showed good agreement of the sensor with manual counting of RR and with electrocardiogram (ECG) measurements of HR.

1. Introduction

Cardiovascular diseases (CVDs) are the main cause of death worldwide, and thus, they constitute a heavy burden on global health systems [1]. Early detection of CVDs is essential, which can effectively slow down the course of the disease. The monitoring of cardiorespiratory activity offers crucial information for preventing health problems, thus promoting the early diagnosis and treatment of cardiovascular and respiratory diseases, such as stroke [2], heart attacks [3], and asthma [4], which account for the death of 22 million people annually including children, adults and elderly people [5]. The respiratory rate (RR) and heart rate (HR) are critical parameters in assessing cardiorespiratory functionalities due to the early warning for serious cardiorespiratory diseases [6].

Until now, the gold standard for heart rate monitoring is the electrocardiogram [7], while respiratory rate is monitored by impedance pneumography [8]. These methods are normally used for monitoring cardiac and respiratory frequency during hospitalization, with some cardiopulmonary diseases already early warning [9]. However, devices for clinical monitoring have limitations in several use scenarios since they do not allow long-term monitoring in daily life. Fortunately, new frontiers in health monitoring have been recently opened due to the Internet of Things revolution. Different technologies are investigated as wearables for cardiorespiratory monitoring, such as strain sensors based on conductive nanomaterials such as carbon nanotubes [10], graphene [11] and nanowires [12], which respond to mechanical deformations by various resistance or capacitance. These electronic sensors are capable of monitoring cardiorespiratory activity but suffer from electromagnetic interferences and electrical safety issues [13].

The rapidly growing optical fiber sensing technology has been investigated for cardiorespiratory monitoring, showing the advantages of immunity to electromagnetic interferences, inherent

electric safety, and excellent multiplexing capabilities [14]. Junior et al. presented a polymethyl-methacrylate (PMMA) plastic optical fiber wearable sensor for the simultaneous measurement of RR and HR, that was based on a polished fiber acting as a curvature sensor to collect the RR and HR by measuring the optical power attenuation caused by the rate of the curvature differences of the wearable part [15]. Xin et al. reported a ZEONEX polymer optical fiber Bragg device embedded in silicone rubber substrate placed on the wrist, to detect heart and respiration rates [16]. Tavares et al. also reported a silica optical fiber Bragg grating embedded in 3D mode as a wearable device for RR and HR monitoring during normal breathing and apnea [17]. To improve the comfort and compactness of the device, Leal-Junior et al. combined sensors with fabrics as smart textiles [18] and investigated multifunctional performance [19], Aitkulov et al. designed smartphone-POF smart textile sensors [20,21], and Issatayeva et al. proposed FBG arrays embedded into elastic belt [22] for RR monitoring. However, most of these optical fiber wearable sensors have been fabricated from glass (silica [17,23]) and stiff plastics (PMMA [15,24], ZEONEX [16,25], etc.). These materials have a relatively high Young's modulus, typically larger than 1 GPa, which practically limits their potential for integrating into clothing so fibers with lower Young's modulus would be desirable for monitoring human physiological and body function. Guo et al. reported an stretchable dye-doped polydimethylsiloxane optical fiber integrated in the body to monitor various human activities which lead to large strain variation, such as joint motion, speaking, and deep breathing, although it is not sufficiently sensitive for cardiac monitoring [26].

In this work, we design an optical fiber sensor consisting of one elastomer optical fiber section between two multimode silica optical fibers, which shows excellent sensitivity and durability. This structure greatly improves the mechanical properties of the optical fiber and increases the feasibility and safety of integrating the optical fiber with fabric. A variety of prototypes are designed, fabricated and tested in order to identify the best model, which was integrated in a belt to allow simultaneous precordial RR and HR signal monitoring and blastocardiography (BCG) signals. Finally, we test the performance of the belt on 10 volunteers, compare RR and HR measurements in various positions, and analyze the accuracy, stability, and agreement with reference methods of the results.

2. Methodology

2.1. Sensor design and fabrication

The sensing probe is based on two thermoset multimode silica optical fibers with an elastomer optical fiber, as depicted in Fig. 1. The bare silica optical fibers are fragile and have a large Young's modulus, i.e. a magnitude in the order of GPa, which means that exhibit high tensile resistance [27]. By contrast, the elastomer optical fiber is made of elastomer tube filled with polydimethylsiloxane (PDMS) which are materials with much smaller Young's modulus, i.e. 10 MPa [28] and 1 ~ 3 MPa [29], respectively. Therefore, the addition of elastomer optical fiber improves the flexibility and extensibility of the sensor, allowing to meet the requirements for subsequent RR and HR monitoring.

The multimode silica optical fibers have a core diameter of 62.5 μm, and a cladding diameter of 125 μm. After cutting them, they were processed to remove the cladding over 10 mm long section for subsequent insertion of the fiber core into the elastomer tube. The PDMS requires a curing agent as a mixture in a ratio of 10:1 by weight and a standing time of 40 minutes. After the PDMS had been completely degassed, it is injected into a 30 mm long silicone elastomer (Cole-Parmer silicone tube with an inner diameter of 0.3 mm and an outside diameter of 0.64 mm). Then, both bare silica optical fiber cores are inserted into each end of the elastomer tube. For high quality sensor fabrication, one of the multimode fibers is fixed first, then, the elastomer tube is inserted horizontally and the other fiber is inserted into the other end of the elastomer tube while it is connected to the light power meter to assure maximum light transmission. Finally, the
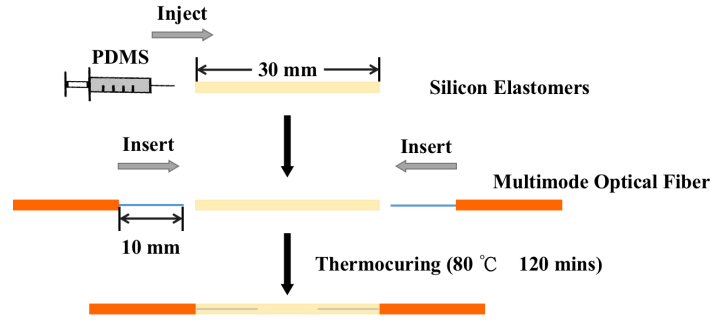
Fig. 1. The structure and fabrication process of the sensor.

whole structure is placed in the heating station (DLAB, MS7-H550-Pro) for 2 hours at 80 °C for thermocuring.

In the following, the theoretical analysis of the propagation of light along the elastomer optical fiber is presented. The intensity losses suffered by light propagating along silica optical fiber sections and by light coupling at both ends are fixed values, so only the losses arisen by the elastomer optical fiber are considered. Moreover, the deformation of the silica optical fiber can be ignored during the experiments since its Young's modulus is much larger than that of elastomer optical fiber. Hence, both the physical strain of the sensor and the loss of light intensity impact on the elastomer optical fiber.

According to Beer-Lambert law, the attenuation of light intensity occurs as it propagates along the elastomer fiber, and the relation between the attenuation and the fiber parameters is given by the following expression:

$$A = \epsilon L c \tag{1}$$

where A is the attenuation, ϵ is the attenuation coefficient of PDMS, L is the length of the elastomer optical fiber and c is the concentration of PDMS. Therefore, P_{in} and P_{out}, as the light power at the input and output, respectively, of the elastomer optical fiber can be related as follows:

$$\frac{P_{in}}{P_{out}} = e^A \tag{2}$$

Let us consider the definition of strain:

$$s = \frac{\Delta L}{L_0} \tag{3}$$

$$L = \Delta L + L_0 \tag{4}$$

where L_0 and ΔL are the original length and the elongation of the elastomer optical fiber, respectively. Then, the following relationship between output light power and strain can be written:

$$P_{out} = P_{in} e^{-\epsilon L_0 c(1+s)} \tag{5}$$

As temperature usually affects the output light intensity slowly [30,31], and frequency information are the main focus for our experiment, so we ignored the temperature influence here. When it comes to the dynamic movement of the optical fiber, it is sometimes necessary to consider the error caused by the viscoelasticity of the material [15]. However, in this study, the hysteresis behavior of strain response caused by viscoelasticity can be neglected due to the high elasticity of PDMS [32]. An elastomer optical fiber was fixed with two 3D X-Y-Z motion stage (Thorlabs MBT616D) and stretched in steps of 0.5 mm. The axial tension applied by the stages determined

the strain change in the experiment. The effective length of the elastomer optical fiber was 10 mm and the strain properties of this fiber were experimentally measured. As shown in Fig. 2(a), the output power was monitored as the strain was increased from 0 to 80%, and the vertical axis takes the form of logarithmic coordinates to visualize the linearity. With the strain increase, the output intensity decreases exponentially, $P_{out} \propto \exp -3.104s$, as expected from Eq. (5).
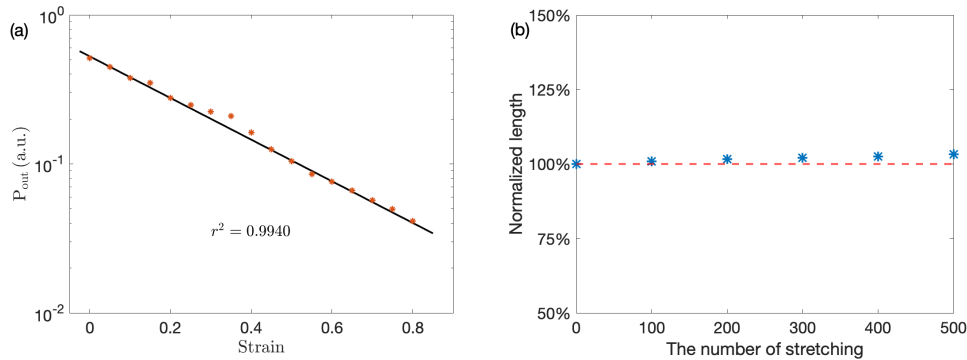

Fig. 2. The properties of the elastomer optical fiber: (a) The relationship between strain and output light intensity; (b) Durability during 500 cycles of stretching and losing with the strain of 50%.

The tensile tester (Handpi Instruments) was employed to measure the durability of the elastomer optical fiber by stretching it hundreds of times under a strain of 50%. The length of the elastomer section was measured after every 100 stretches and define normalized length as $L/L_0 \times 100\%$, and the test results are shown in Fig. 2(b), indicating almost no change in the length while after 500 repetitions the relative deformation of the elastomer is only 3.24%.

2.2. *Prototype design*

Since the sensor needs to be in contact with the human body to get proper measurements, this section aims to investigate a wearable sensor based on the stretchable optical fiber. Note that the body micro-vibrations caused by breathing and heartbeat are not a simple linear motion. The surface of the body is curved and thus, the elastomer optical fiber would bend if the sensor is worn directly. In this case, the fiber end faces would not keep aligned, which adds a random factor with loss of repeatability in optical signal monitoring. In response to this problem, two prototypes were designed to limit the movement of the elastomer section of the optical fiber.

The prototypes are shown schematically in Fig. 3 and were made of resin or aluminum alloy. The elastomer optical fiber was inserted into the notch of the prototype so that the elastomer optical fiber is stretched within the fixed notch. Thus, the elastomer optical fiber only undergoes linear deformation and the two ends of the silica optical fiber remain parallel during the deformation process of elastomer optical fiber. Therefore, the prototype improves the repeatability of the elastomer optical fiber stretches and the mechanical stability of the device [33]. Meanwhile, the prototype can also play a role in protecting the optical fiber and improving the mechanical strength of the sensor [34].

2.3. *Belt design*

The design of the belt and the image of the real object is shown in Fig. 4. The central part of the belt is a central elastic fabric with a length of 6 cm and a non-elastic fabric sewn on both sides. This structure allows the stretch deformation of the belt to be provided only by the elastic fabric. The elastomer optical fiber is attached to the elastic part of the belt, while the rest of the
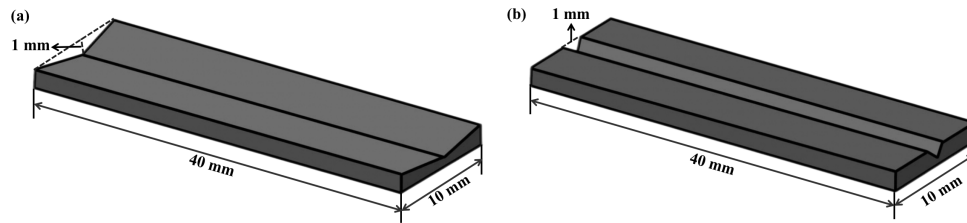
Fig. 3. Schematic Diagrams of prototypes: (a) Broad wedge notch; (b) Narrow wedge notch.

optical fiber is fixed to the non-elastic part of the belt, the deformation of the belt drives the optical fiber to stretch. In this case, the changes in the optical fiber are merely provided by the elastomer. This structure maximizes the utility of strain, magnifies the local strain and facilitates the measurement of small deformations caused by the human body. The prototype is stitched to the belt, which can limit the activity of the optical fiber and protect the sensor to some extent.
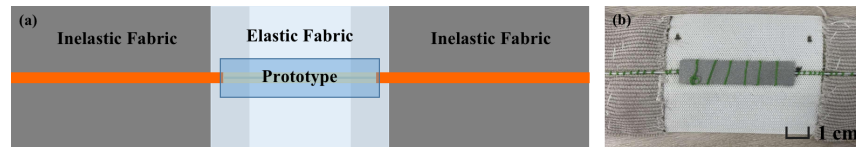

Fig. 4. The belt design: (a) Schematic diagram; (b) Photograph.

2.4. General system design

The schematic diagram of the experimental characterization setup is illustrated in Fig. 5, which includes a superluminiscent diode (SLD) light source (SUPERLUM, SLD-Mcs-371-HP2-SM), the belt knitted with the elastomer optical fiber and an Optical Spectra Analyzer (OSA) consisting of a compact spectrometer (THORLABS, CCS175) and Thorlabs OSA software. The output light intensity of the spectrometer can be recieved by calculating the mean value of the light intensity in the analyzed wavelength interval using Thorlabs OSA software, while the Long-Term Analysis tool of Thorlabs OSA software enables the long-term monitoring of the light intensity. The belt is worn over the chest and the elastic part is worn over the precordial area. Physiological activities such as respiration and heartbeat cause the physical deformation of the chest and thus, the sensor undergoes physical deformation, namely the optical path length L of the elastomer optical fiber length changes. Accordingly, when the light is transmitted along the sensing area, according to Eq. (5), the intensity of the output light varies, as will be recorded by the spectrometer. The system has the potential for portability, by integrating the belt with PD and Bluetooth [35] or with a smartphone [36] to form a portable version.

2.5. Data process

Data processing can be mainly divided into two parts: filtering and time-frequency domain analysis. The flow diagram of this process is shown in Fig. 6, since the frequency bands of different physiological signals at resting state are already known, from 10 bpm to 24 bpm (roughly corresponding to 0.1 Hz to 0.4 Hz) for respiratory rate (RR) [37,38] and from 50 bpm to 100 bpm (roughly corresponding to 0.8 Hz to 1.6 Hz) for heart rate (HR) [39,40]. The BCG signal indicates a micro-movement of the body surface due to blood pulsation, namely BCG signal is associated with heartbeat activity [41]. The frequency band of 1 Hz to 12 Hz contains information on the main characteristics of BCG. The filtering part mainly uses Butterworth digital, in the
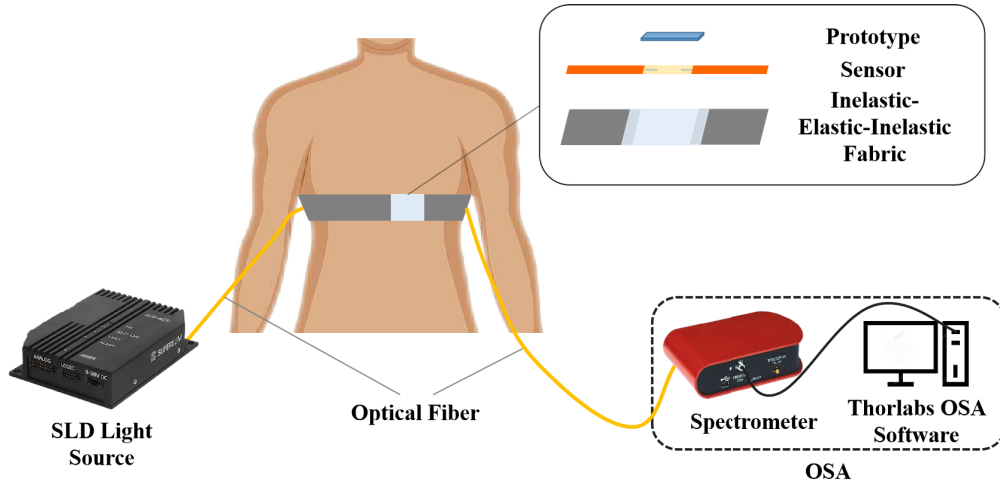
Fig. 5. Experimental schematic diagram.

experiment, a combination of a high-pass, a low-pass, and a band-pass Butterworth filters were employed to obtain more accurate respiratory and heart signals.
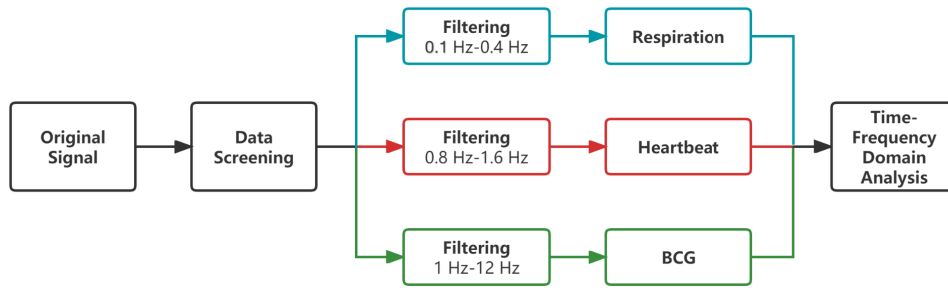

Fig. 6. Flow diagram for data processing.

Respiratory and heartbeat signals are not stationary, so Short-time Fourier Transform (STFT) is used for time-frequency domain analysis.

$$S(f) = \int_{-\infty}^{\infty} w(t' - t)s(t')e^{-2j\pi f t'} \, \mathrm{d}t' \tag{6}$$

where s is the original time domain signal, $S(f)$ is the frequency domain signal, and w is the window function. Since the experimental data are discrete, the discrete STFT is used in the data analysis, as follows:

$$S(f) = \sum_{n=0}^{N-1} s(n + m)w(n)e^{-j\frac{2\pi}{N}fn} \tag{7}$$

where m denotes the offset and N is the length of the window. For the window function, based on the large difference in amplitude of the RR and HR, the Blackman window [42] with large stop-band attenuation is chosen in the data process:

$$w_{Blackman}(n) = 0.42 - 0.5\cos\frac{2\pi n}{N} + 0.08\cos\frac{4\pi n}{N}, \quad 0 \leqslant n \leqslant N \tag{8}$$

3. Experiments and discussion

3.1. Prototype select

Different prototypes were assessed in terms of the coefficient of variation (CV) k_v and coefficient k, which are defined to evaluate the stability and the magnification of the signal, respectively, as follows:

$$k_v = \frac{\sigma}{E} \tag{9}$$

$$k_v = \sqrt{k_{vr}^2 + k_{vh}^2} \tag{10}$$

$$k = \frac{A_H}{A_R} \tag{11}$$

where σ and E are standard deviations and expectation values of RR or HR, respectively. The total coefficient of variation is defined in Eq. (10) by combining RR and HR, where k_{vr} and k_{vh} are CV of RR and HR, and smaller k_v means better stability [43]. With regards to the definition of k are shown in Eq. (11), A_R and A_H are the amplitudes of the respiratory and the heartbeat peaks, respectively.

In the following, four prototypes with different structures are shown in Fig. 3, all of them were manufactured by 3D printing (CREALITY, CR-3040 Pro): A prototype (aluminium alloy, 1.5 mm high, narrow wedge notch), B prototype (aluminium alloy, 2 mm high, broad wedge notch), C prototype (resin, 1.5 mm high, narrow wedge notch) and D prototype (resin, 3 mm high, narrow wedge notch). A volunteer wore the belt with the different prototypes and also with the sensor without any prototype. Each prototype was measured 10 times, and the duration of each measurement is 30 s. The obtained data were selected by quartile method and then, the parameters k_v and k were calculated as detailed in Table 1.

Table 1. Test results for belts with and without different prototypes.

	A	B	C	D	without prototype
k_v	0.1312	0.1613	0.1376	0.1762	0.3403
k	0.0747	0.0459	0.0433	0.0597	0.0071

From Fig. 7, we found for both RR and HR, the belts with prototypes are better than the belt without prototype. Table 1 also shows that the belt with the A-prototype exhibits the best results with the smallest k_v and the largest k. Therefore, the A-prototype (aluminum alloy, 1.5 mm high, narrow wedge notch) is considered to be the best prototype, and all subsequent experiments would be completed by using the sensor with the A-prototype.
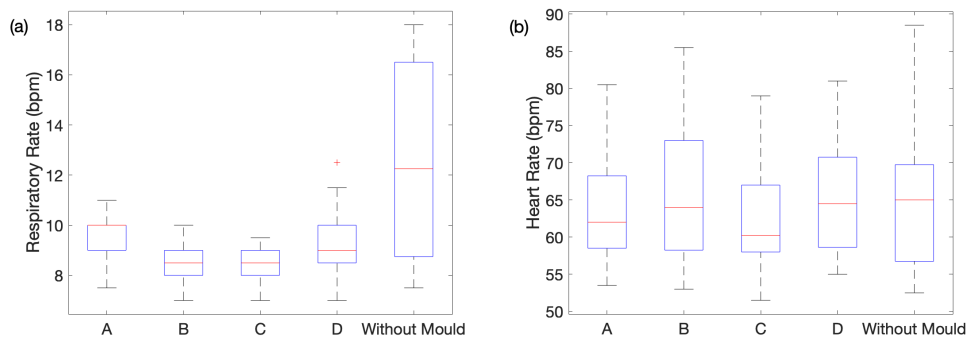

Fig. 7. Box diagram of test results: (a) RR; (b) HR.

3.2. HR and BR monitoring

One volunteer (male, age 21, 167 cm, and 60 kg) was required to wear the belt at the area of the apical impulse. The apical impulse is roughly at the fifth intercostal space of the left midclavicular line, where the palpable cardiac impulse is held [44]. The volunteer put on the belt and lied flat on the mattress to start the measurement, and light intensity was measured continuously using Long-term Analysis with Thorlabs OSA software at a sampling rate of 10, which lasted for 1 min.

Clear periodic variation can be obtained from the measured intensity signal, as displayed in Fig. 8(a). While breathing, there is a large variation in chest circumference, hence respiratory activity can be seen directly from the raw intensity signal. During inhalation, the chest circumference lengthens and the elastomer optical fiber part stretches, leading to a decrease in light intensity. The process of exhalation is opposite, since the chest circumference shortens, the elastomer optical fiber part is released and the light intensity increases. The variation in amplitude is related to the depth of respiration. However, the mechanical variations caused by the heart beating are much weaker than those caused by respiration, and thus, cardiac information is submerged in the respiratory activity as appears in the measured intensity signal. Therefore, the heartbeat-related information must be separated by signal processing.
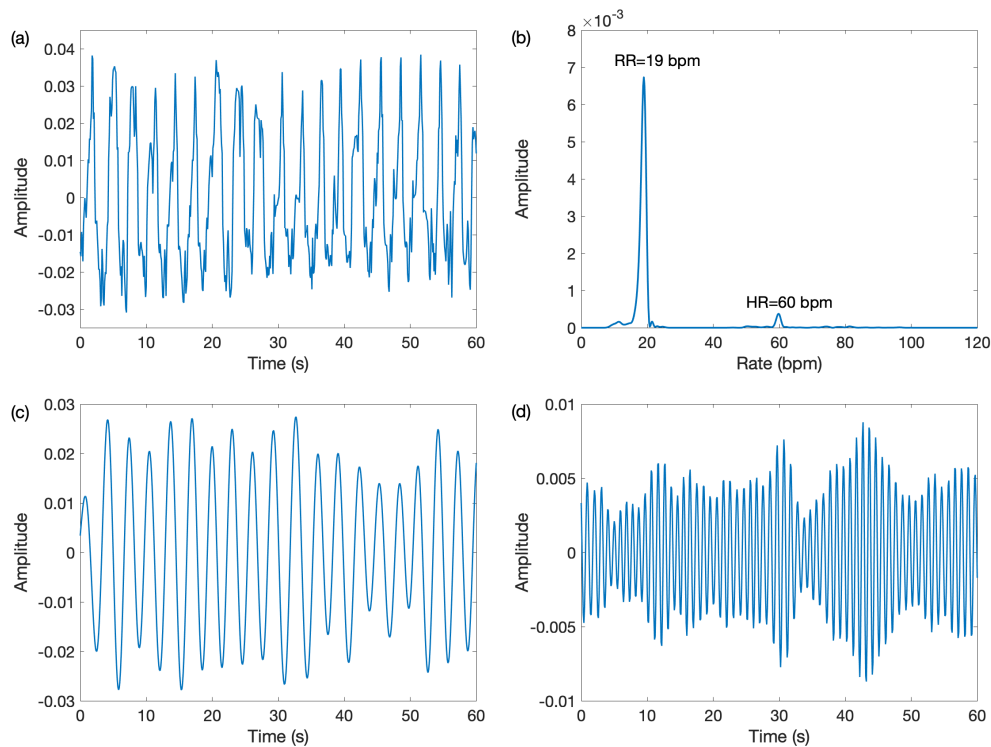

Fig. 8. Time and frequency domain analysis of light intensity signals: (a) Original intensity signal; (b) Frequency domain figure after filtration and STFT; (c) Breath time domain; (d) Heartbeat time domain.

The original signal collected by OSA was filtered using the Butterworth filter for both respiratory rate and heart rate bands. Afterwards, we filtered the harmonics of RR through FIR digital filter and use STFT to analyze the filtered signal in the frequency domain. From Fig. 8(b), the physical changes in the chest lead to two distinct peaks in the frequency, one of which is located in the respiratory frequency window with a rate of 19 bpm, which is the measured RR.

The other is situated in the heart rate frequency window with a rate of 60 bpm, which is the value of measured cardiac beat frequency. For the time domain analysis, the high harmonics of RR in the original signal were filtered by FIR filter, and then, the time domain signals were separated by digital Butterworth filters within RR and HR bands. After filtering each one of the bands, Fig. 8(c) and Fig. 8(d) show the signals corresponding of respiratory activity and cardiac beat in the time domain. Compared to Fig. 8(a) and Fig. 8(c), the respiratory waveform is similar to the original collected signal and they vary in the same trend, which illustrates, at least to some extent, the accuracy of the respiratory measurements and the feasibility of the data processing method.

3.3. BCG monitoring

BCG is a weak mechanical signal produced by the heart pumping activity that causes the body to vibrate synchronously [45]. The BCG signal consists of several peak signals, namely G, H, I, J, K, L, and M peaks, which have different physiological significance [46]. For example, H, I, J, and K peaks are associated with cardiac contraction while M and N waves are related to cardiac diastole [45]. Our proposed belt was also used for BCG measurement and the electrocardiogram (ECG) was measured simultaneously to facilitate the determination of the BCG signal. Three electrodes of the ECG measurement module are worn on the subject's left chest, right subcostal, and left hypogastrium. A volunteer (female, age 21, 163 cm and 50 kg) wore the belt and electrodes simultaneously and measurements were taken in lying position. The OSA is used for light intensity acquisition with sampling rate set to 100 and the measurement duration was 1 minute.

　　Figure 9 indicate the measured BCG signal obtained from the original light intensity signal filtered by a bandpass frequency window of 1-12 Hz. Figure 9(a) shows the BCG signal while Fig. 9(b) shows one of the segments, where most of the characteristics of the BCG signal, i.e. H, I, J, K, and L peaks are clear. That proves the proposed sensor is also valid for BCG signal measurement. Figure 9(c) shows a comparison of ECG and BCG signals, both of which are relevant for cardiac activity. The RJ interval is the interval between the J-peak of BCG and the R-peak of ECG, the most widely measured time interval based on BCG, is relatively stable and is related to heart activity such as systolic blood pressure [47]. HR can be estimated by measuring the J-peak interval in the BCG signal, and the results of ECG and BCG measurements are shown in the Table 2, where the absolute error ϵ is between 0 and 5 bpm.

Table 2. HR measured using ECG and HR estimated using BCG.

ECG (bpm)	BCG (bpm)	ϵ (bpm)
63	63	0
64	69	5
62	58	4
68	72	4
66	63	3
68	69	1

3.4. Different position test

The following experiments involve 10 volunteers (5 males and 5 females). All of them are in the age range of 22 ± 2, and their other physiological information are shown in Table 3. Each volunteer was measured under three states in turn: standing, sitting, and lying state. Each state was measured ten times serially during 30 s. Experimental signals were processed in a similar way as in the previous part, and the results are shown in Fig. 10.
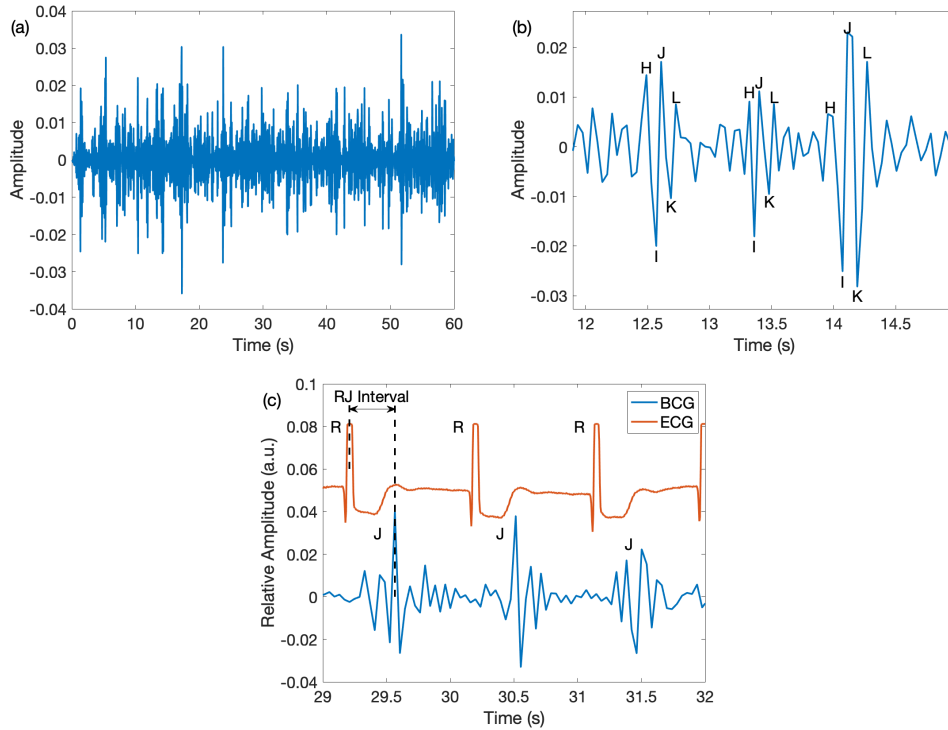
Fig. 9. BCG signal: (a) BCG signal for 1 min; (b) A single BCG signal; (c) A comparison between ECG and BCG.
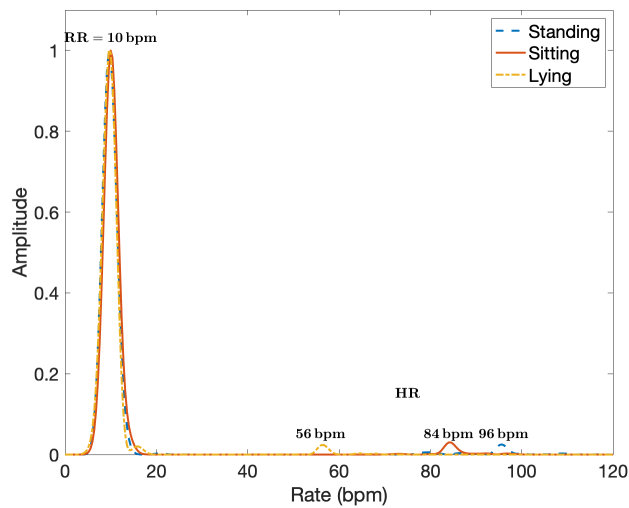

Fig. 10. Comparison of breathing and heart rate monitoring in different body positions. Taking the measurements of Female 4 as an example, RR remained at 10 bpm, but HR in standing, sitting and lying positions were 96 bpm, 84 bpm, and 56 bpm respectively.

Table 3. Physiological information for volunteers.

Index	Height (cm)	Weight (kg)
Female 1	155	59
Female 2	163	50
Female 3	161	44
Female 4	173	65
Female 5	170	56
Male 1	178	80
Male 2	172	61
Male 3	164	58
Male 4	166	56
Male 5	173	62

The results indicate that our sensor can accurately measure breathing and heart rate at different body positions. Figure 10 is the normalized frequency domain signal arisen from the physical deformation of the chest in standing, sitting, and lying positions. For different body positions, the sensor has good performance in the resting state of the body. Comparing the frequency domain plots of these three body positions, we confirmed that in the resting state, the RR does not change much in different positions, whereas the HR changed largely in the resting state. The variation in HR was specifically demonstrated by the greatest HR in the standing position and the smallest in the lying position, which is related to hormonal and neurological regulation [48]. However, the difference in HR among the three positions is different for each individual, in other words, we can identify the body states of each individual by this difference.

3.5. Analysis

This section discusses the accuracy, stability, and the agreement with professional medical equipment of the proposed wearable stretchable optical fiber sensor. The Mean Absolute Percentage Error (MAPE) and Root Mean Square Error (RMSE) metrics implemented to analyze the accuracy and stability of the measured RR and HR, and used the Bland-Altman method to analyze the agreement [49]. As it is well known, the MAPE and RMSE can be calculated as follows:

$$MAPE = \frac{1}{n} \sum_{i=1}^{n} \left| \frac{X_i - X_{i0}}{X_{i0}} \right| \times 100\% \tag{12}$$

$$RMSE = \sqrt{\frac{1}{n} \sum_{i=1}^{n} (X_i - X_{i0})^2} \tag{13}$$

$$Y_W = \sqrt{Y_R^2 + Y_H^2} \tag{14}$$

where X refers to respiratory or heart activity, the footnote $_i$ and $_{i0}$ denote the measured and reference values respectively, and n indicates the number of measurements. Y can refer to MAPE or RMSE, which are used to calculate the weighted MAPE and RMSE considering both respiration and heart rate.

We measured the RR and HR of 10 volunteers shown in Table 3 in their resting state in different body positions (standing, sitting, and lying). Each subject in each position was measured 10 times for 30 seconds each, and finally, 300 sets of respiratory rate and heart rate data are obtained by processing the original light intensity signal. The reference method for RR is manual counting [50] and the reference data for HR is from pulse oximeter (CONTEC, CMS60D). These data

were processed by using Eq. (12), Eq. (13) and Eq. (14) to analyze the accuracy and stability of the measurements, and the results are shown in Table 4 and Table 5. In general, overall average weighted MAPE and RMSE of 5.25 % and 1.28 bpm, respectively. For both sexes, weighted MAPE is within roughly 5% plus or minus 2% and weighted RMSE is between 1 bpm and 1.5 bpm, hence the device is suitable for both men and women. In terms of accuracy, there is no obvious difference between respiratory rate and heart rate monitoring among different body positions. And the MAPE of HR is much smaller than that of RR, so the accuracy of heart rate monitoring is significantly better than that of respiration. However, the maximum deviation of RR and HR are respectively 1 bpm and 3 bpm. This contradiction occurs because the real value of RR is much smaller than that of HR. For the stability of the device, the RMSE of RR is significantly smaller than that of HR, so the stability of respiratory rate monitoring is better than that of heart rate monitoring. For the measurement of RR, different body positions lead to similar RMSE, namely body position is a slight influencing factor for measurement stability. But for HR, the stability in the lying position is better than that in other body positions probably due to less micro-movements of the body in the lying position so the equipment is less affected by the environment.

Table 4. MAPE.

Index	RR(%)				HR(%)				Weighted
	Stand	Sit	Lie	Average	Stand	Sit	Lie	Average	
Female 1	2.65	2.21	9.42	4.76	1.23	1.95	1.49	1.56	5.01
Female 2	2.21	3.25	2.82	2.76	1.21	0.72	1.24	1.06	2.96
Female 3	3.68	2.95	3.62	3.42	2.17	1.69	1.03	1.63	3.79
Female 4	7.15	5.28	4.45	5.63	1.29	1.59	1.30	1.39	5.80
Female 5	5.48	5.31	6.57	5.79	1.39	1.38	1.48	1.42	5.96
Male 1	6.63	6.26	8.68	7.19	1.64	1.26	1.31	1.40	7.33
Male 2	5.65	4.62	5.16	5.14	1.18	1.34	1.12	1.21	5.28
Male 3	7.95	4.97	2.03	4.98	1.87	1.73	1.25	1.62	5.24
Male 4	4.65	5.07	4.25	4.66	1.62	1.23	0.87	1.24	4.82
Male 5	6.79	5.21	6.58	6.19	1.42	1.39	1.45	1.42	6.35

Table 5. RMSE.

Index	RR (bpm)				HR (bpm)				Weighted
	Stand	Sit	Lie	Average	Stand	Sit	Lie	Average	
Female 1	0.31	0.35	0.55	0.40	1.17	1.62	1.14	1.31	1.37
Female 2	0.21	0.28	0.34	0.28	1.45	0.76	1.03	1.08	1.11
Female 3	0.45	0.35	0.43	0.41	1.80	1.32	0.79	1.30	1.37
Female 4	0.51	0.31	0.33	0.38	1.51	1.36	0.94	1.27	1.32
Female 5	0.47	0.38	0.40	0.42	1.25	1.31	0.94	1.17	1.24
Male 1	0.32	0.41	0.45	0.39	1.49	1.20	1.07	1.26	1.32
Male 2	0.58	0.53	0.50	0.54	1.34	1.17	0.96	1.16	1.28
Male 3	0.66	0.62	0.27	0.52	1.26	1.18	0.74	1.06	1.18
Male 4	0.26	0.34	0.34	0.31	1.62	1.23	0.87	1.24	1.28
Male 5	0.74	0.56	0.66	0.65	1.38	1.14	1.01	1.18	1.35

Bland-Altman is used to analyze the agreement between experimental measurements and the reference device measurements. Bland-Altman plots can be used to visually determine

whether new techniques can replace established methods based on the good agreement between them [51]. In the experiment, all volunteers were required to wear both the experimental and reference equipment and take measurements in the lying position. The reference method for respiratory measurements was manual counting, while the respiratory signal was used for general Bland-Altman analysis since it was relatively stable over time. Thirty volunteers were recruited and 30 sets of respiratory data were measured for 30 seconds each. The reference device for HR measurements is ECG, which was measured in the same way as in the section 3.3 and the new wearable stretchable optical fiber sensor is worn on the subject's apical pulse location. Due to the temporal instability of the HR [52], we believe that independent measurements of individual subjects at different times still satisfy the conditions for the use of the Bland-Altman method [53]. Simultaneous continuous measurements of both devices are carried out in 30 sets of 30 seconds each. The ECG signal is directly processed by the time-frequency domain analysis to obtain the subject's HR, and the light intensity signal is filtered and then analyzed similarly. The data obtained from the ECG measurements were used as a reference value. The mean of the differences μ and the limits of agreement (LoA) are two very important parameters in Bland-Alman method, whose definitions are shown in Eq. (15) and Eq. (16), where n is number of measurements, X_i and X_{i0} are respectively measurement and reference value, and σ is the standard deviation in Eq. (17).

$$\mu = \frac{1}{n} \sum_{i=1}^{n} (X_i - X_{i0}) \tag{15}$$

$$LoA = \mu \pm 1.96\sigma \tag{16}$$

$$\sigma = \sqrt{\frac{\sum_{i=1}^{n} (X_i - X_{i0} - \mu)^2}{n - 1}} \tag{17}$$

The Bland-Altman diagrams are plotted for RR and HR as shown in Fig. 11. The LoA in Fig. 11(a) is -1.0525 bpm and 0.6025 bpm, and the RR measured by the test belt is within the LoA ranges, which indicates that the belt is in good agreement with manual counting method. From Fig. 11(b), the mean of the difference between the two methods of measuring heart rate was -0.5299 bpm, with a maximum difference of 4 bpm and LoA of -3.1548 bpm and 2.0949 bpm, with 93.3% (28/30) of the measurements falling within this range, indicating good agreement with ECG method. Figure 11(b) also shows that the data points are uniformly distributed, suggesting that there is no significant different between the measured values.
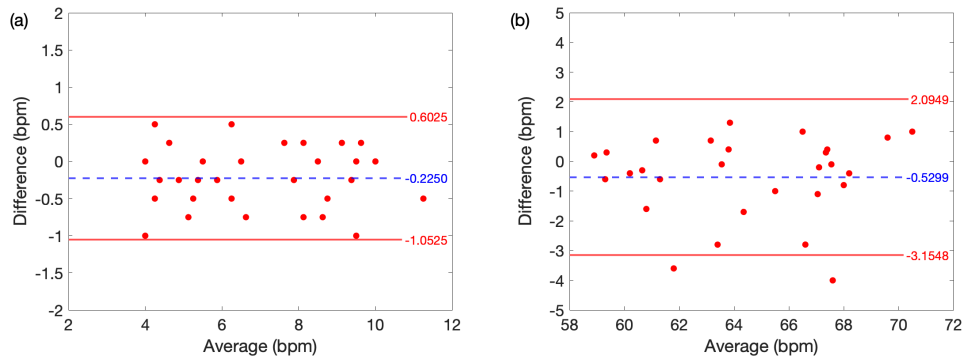

Fig. 11. Bland-Altman figure: (a) The agreement analysis of RR; (b) The agreement analysis of HR. The horizontal axis is the average of the reference and measured values and the vertical axis shows the difference between them. The dot line is μ and the solid line is LoA.

4. Conclusion

In this study, we designed and fabricated a wearable stretchable optical fiber sensor with a structure consisting of an elastomer optical fiber sandwiched by two multimode silica optical fiber. To enable RR and HR monitoring, we integrated the wearable stretchable optical fiber sensor with a prototype with a narrow wedge notch sewn onto the belt to constrain the movement of the elastomer optical fiber. The device allows simultaneous monitoring of RR, HR and BCG, as well as RR and HR in different body positions at resting state. To test the performance of the device, we compared RR and HR measurements using manual counting methods and pulse oximeter, respectively. Results from 10 subjects show that the device has good measurement accuracy, stability and agreement, in which HR in lying position can be within 1.5% of MAPE, and RR can be around 0.5 bpm of RMSE. The addition of the elastomer optical fiber enhances the physical properties of the sensor, making it easier to attach to the fabric. Therefore, the proposed sensor has great potential for biomedical and wearable applications.

Disclosures. The authors declare no conflicts of interest.

Data Availability. The data that support the findings of this study are available from the corresponding author upon reasonable request.

References

1. WHO, "Noncommunicable diseases," World Health Organization (2022) [retrieved 24 March 2023], https://www.who.int/news-room/fact-sheets/detail/noncommunicable-diseases.
2. L. Luo, H. Meng, Z. Wang, S. Zhu, S. Yuan, Y. Wang, and Q. Wang, "Effect of high-intensity exercise on cardiorespiratory fitness in stroke survivors: A systematic review and meta-analysis," Ann. Phys. Rehabil. Med. **63**(1), 59–68 (2020).
3. H. V. Huikuri and P. K. Stein, "Heart rate variability in risk stratification of cardiac patients," Prog. Cardiovasc. Dis. **56**(2), 153–159 (2013).
4. J. Milagro, J. Gracia-Tabuenca, V.-P. Seppä, J. Karjalainen, M. Paassilta, M. Orini, R. Bailón, E. Gil, and J. Viik, "Noninvasive cardiorespiratory signals analysis for asthma evolution monitoring in preschool children," IEEE Trans. Biomed. Eng. **67**(7), 1863–1871 (2019).
5. WHO, "Cardiovascular diseases (cvds)," World Health Organization (2021) [retrieved 24 March 2023], https://www.who.int/news-room/fact-sheets/detail/cardiovascular-diseases-(cvds).
6. W. W. Labaki and M. K. Han, "Chronic respiratory diseases: a global view," The Lancet Respir. Med. **8**(6), 531–533 (2020).
7. J. J. van Vonderen, S. B. Hooper, J. K. Kroese, A. A. Roest, I. C. Narayen, E. W. van Zwet, and A. B. te Pas, "Pulse oximetry measures a lower heart rate at birth compared with electrocardiography," The J. Pediatr. **166**(1), 49–53 (2015).
8. S. Ansari, K. R. Ward, and K. Najarian, "Motion artifact suppression in impedance pneumography signal for portable monitoring of respiration: An adaptive approach," IEEE Journal of Biomedical and Health Informatics **21**(2), 387–398 (2017).
9. M. Weenk, H. van Goor, B. Frietman, L. J. Engelen, C. J. van Laarhoven, J. Smit, S. J. Bredie, and T. H. van de Belt, "Continuous monitoring of vital signs using wearable devices on the general ward: Pilot study," JMIR Mhealth Uhealth **5**(7), e91 (2017).
10. V. Trovato, E. Teblum, Y. Kostikov, A. Pedrana, V. Re, G. D. Nessim, and G. Rosace, "Sol-gel approach to incorporate millimeter-long carbon nanotubes into fabrics for the development of electrical-conductive textiles," Mater. Chem. Phys. **240**, 122218 (2020).
11. S. Xia, M. Wang, and G. Gao, "Preparation and application of graphene-based wearable sensors," Nano Res. **15**(11), 9850–9865 (2022).
12. K. Wang, L. W. Yap, S. Gong, R. Wang, S. J. Wang, and W. Cheng, "Nanowire-based soft wearable human–machine interfaces for future virtual and augmented reality applications," Adv. Funct. Mater. **31**(39), 2008347 (2021).
13. P. Roriz, L. Carvalho, O. Fraz ao, J. L. Santos, and J. A. Sim oes, "From conventional sensors to fibre optic sensors for strain and force measurements in biomechanics applications: A review," J. Biomech. **47**(6), 1251–1261 (2014).
14. C. Massaroni, M. Zaltieri, D. L. Presti, A. Nicolò, D. Tosi, and E. Schena, "Fiber bragg grating sensors for cardiorespiratory monitoring: A review," IEEE Sens. J. **21**(13), 14069–14080 (2020).

15. A. Leal-Junior, C. R. Díaz, C. Leit ao, M. J. Pontes, C. Marques, and A. Frizera, "Polymer optical fiber-based sensor for simultaneous measurement of breath and heart rate under dynamic movements," Opt. Laser Technol. **109**, 429–436 (2019).

16. X. Cheng, D. S. Gunawardena, C.-F. J. Pun, J. Bonefacino, and H.-Y. Tam, "Single nanosecond-pulse production of polymeric fiber bragg gratings for biomedical applications," Opt. Express **28**(22), 33573–33583 (2020).

17. C. Tavares, C. Leit ao, D. L. Presti, M. Domingues, N. Alberto, H. Silva, and P. Antunes, "Respiratory and heart rate monitoring using an fbg 3d-printed wearable system," Biomed. Opt. Express **13**(4), 2299–2311 (2022).

18. L. Avellar, C. Stefano Filho, G. Delgado, A. Frizera, E. Rocon, and A. Leal-Junior, "Ai-enabled photonic smart garment for movement analysis," Sci. Rep. **12**(1), 4067 (2022).

19. A. Leal-Junior, L. Avellar, V. Biazi, M. S. Soares, A. Frizera, and C. Marques, "Multifunctional flexible optical waveguide sensor: on the bioinspiration for ultrasensitive sensors development," Opto-Electron Adv **5**(10), 210098 (2022).

20. A. Aitkulov and D. Tosi, "Design of an all-pof-fiber smartphone multichannel breathing sensor with camera-division multiplexing," IEEE Sensors Letters **3**(5), 1–4 (2019).

21. A. Aitkulov and D. Tosi, "Optical fiber sensor based on plastic optical fiber and smartphone for measurement of the breathing rate," IEEE Sens. J. **19**(9), 3282–3287 (2019).

22. A. Issatayeva, A. Beisenova, D. Tosi, and C. Molardi, "Fiber-optic based smart textiles for real-time monitoring of breathing rate," Sensors **20**(12), 3408 (2020).

23. T. Li, Y. Su, F. Chen, H. Zheng, W. Meng, Z. Liu, Q. Ai, Q. Liu, Y. Tan, and Z. Zhou, "Bioinspired stretchable fiber-based sensor toward intelligent human–machine interactions," ACS Appl. Mater. Interfaces **14**(19), 22666–22677 (2022).

24. X. Hu, Z. Chen, X. Cheng, R. Min, H. Qu, C. Caucheteur, and H.-Y. Tam, "Femtosecond laser point-by-point bragg grating inscription in bdk-doped step-index pmma optical fibers," Opt. Lett. **47**(2), 249–252 (2022).

25. G. Woyessa, A. Fasano, C. Markos, A. Stefani, H. K. Rasmussen, and O. Bang, "Zeonex microstructured polymer optical fiber: fabrication friendly fibers for high temperature and humidity insensitive bragg grating sensing," Opt. Mater. Express **7**(1), 286–295 (2017).

26. J. Guo, M. Niu, and C. Yang, "Highly flexible and stretchable optical strain sensing for human motion detection," Optica **4**(10), 1285–1288 (2017).

27. X. Luan, X. Xu, M. Li, R. Yu, Q. Zhang, S. Zhang, and L. Cheng, "Design, preparation, and properties of a boron nitride coating of silica optical fiber for high temperature sensing applications," J. Alloys Compd. **850**, 156782 (2021).

28. MatWeb, "Overview of materials for silicone rubber," Material Property Data [retrieved 2 February 2023], https://www.matweb.com/search/DataSheet.aspx?MatGUID=cbe7a469897a47eda563816c86a73520.

29. M. P. Wolf, G. B. Salieb-Beugelaar, and P. Hunziker, "Pdms with designer functionalities–properties, modifications strategies, and applications," Prog. Polym. Sci. **83**, 97–134 (2018).

30. A. Leal-Junior, C. Marques, A. Frizera, and M. J. Pontes, "Dynamic mechanical analysis on a polymethyl methacrylate (PMMA) polymer optical fiber," IEEE Sens. J. **18**(6), 2353–2361 (2018).

31. A. Leal-Junior, L. Avellar, A. Frizera, and C. Marques, "Smart textiles for multimodal wearable sensing using highly stretchable multiplexed optical fiber system," Sci. Rep. **10**(1), 13867 (2020).

32. S. Deguchi, J. Hotta, S. Yokoyama, and T. S. Matsui, "Viscoelastic and optical properties of four different PDMS polymers," J. Micromech. Microeng. **25**(9), 097002 (2015).

33. P. Mishra, K. Chatterjee, H. Kumar, and R. Jha, "Flexible and wearable photonic-crystal fiber interferometer for physiological monitoring and healthcare," ACS Appl. Opt. Mater. **1**(2), 569–577 (2023).

34. P. Mishra, H. Kumar, S. Sahu, and R. Jha, "Flexible and wearable optical system based on u-shaped cascaded microfiber interferometer," Adv. Mater. Technol. **8**(3), 2200661 (2023).

35. C. A. R. Diaz, A. G. Leal-Junior, L. M. Avellar, P. F. C. Antunes, M. J. Pontes, C. Marques, A. Frizera, and M. R. N. Ribeiro, "Perrogator: A portable energy-efficient interrogator for dynamic monitoring of wavelength-based sensors in wearable applications," Sensors **19**(13), 2962 (2019).

36. L. G. Gomes, R. de Mello, and A. Leal-Junior, "Respiration frequency rate monitoring using smartphone-integrated polymer optical fibers sensors with cloud connectivity," Opt. Fiber Technol. **78**, 103313 (2023).

37. M. A. Cretikos, R. Bellomo, K. Hillman, J. Chen, S. Finfer, and A. Flabouris, "Respiratory rate: the neglected vital sign," Med. J. Aust. **188**(11), 657–659 (2008).

38. S. R. Braun, *Chapter 43 - Respiratory Rate and Pattern* (Butterworths, 1990), pp. 226–230.

39. D. H. Spodick, "Redefinition of normal sinus heart rate," Chest **104**(3), 939–941 (1993).

40. T. W. Hansen, L. Thijs, and J. Boggia, *et al.*, "Prognostic value of ambulatory heart rate revisited in 6928 subjects from 6 populations," Hypertension **52**(2), 229–235 (2008).

41. M. Marino, Q. Liu, V. Koudelka, C. Porcaro, J. Hlinka, N. Wenderoth, and D. Mantini, "Adaptive optimal basis set for bcg artifact removal in simultaneous eeg-fmri," Sci. Rep. **8**(1), 8902 (2018).

42. R. B. Blackman and J. W. Tukey, "The measurement of power spectra from the point of view of communications engineering–part i," Bell Syst. Tech. J. **37**(1), 185–282 (1958).

43. O. Shechtman, *The Coefficient of Variation as an Index of Measurement Reliability* (Springer Berlin Heidelberg, 2013), pp. 39–49.

44. S. McGee, *Chapter 38 - Palpation of the Heart* (Elsevier, 2018), pp. 317–326.e2.

45. R. Casanella, J. Gomez-Clapers, and R. Pallas-Areny, "On time interval measurements using bcg," in *2012 Annual International Conference of the IEEE Engineering in Medicine and Biology Society*, (2012), pp. 5034–5037.

46. J. Lin, R. Fu, X. Zhong, P. Yu, G. Tan, W. Li, H. Zhang, Y. Li, L. Zhou, and C. Ning, "Wearable sensors and devices for real-time cardiovascular disease monitoring," Cell Reports Phys. Sci. **2**, 100541 (2021).

47. S. Chen, F. Tan, W. Lyu, and C. Yu, "Ballistocardiography monitoring system based on optical fiber interferometer aided with heartbeat segmentation algorithm," Biomed. Opt. Express **11**(10), 5458–5469 (2020).

48. K. Hnatkova, M. Šišáková, P. Smetana, O. Toman, K. M. Huster, T. Novotný, G. Schmidt, and M. Malik, "Sex differences in heart rate responses to postural provocations," Int. J. Cardiol. **297**, 126–134 (2019).

49. M. Harford, J. Catherall, S. Gerry, J. Young, and P. Watkinson, "Availability and performance of image-based, non-contact methods of monitoring heart rate, blood pressure, respiratory rate, and oxygen saturation: a systematic review," Physiological Measurement **40**(6), 06TR01 (2019).

50. S. Wang, M. Liu, B. Pang, P. Li, Z. Yao, X. Zhang, and H. Chen, "A new physiological signal acquisition patch designed with advanced respiration monitoring algorithm based on 3-axis accelerator and gyroscope," in *2018 40th Annual International Conference of the IEEE Engineering in Medicine and Biology Society (EMBC)*, (2018), pp. 441–444.

51. P. S. Myles and J. Cui, "I. Using the Bland–Altman method to measure agreement with repeated measures," BJA: Br. J. Anaesth. **99**(3), 309–311 (2007).

52. G. Billman, "Heart rate variability – a historical perspective," Front. Physiol. **2**, 86 (2011).

53. R. Jaros, J. Nedoma, S. Kepak, and R. Martinek, "Fiber-optic interferometry-based heart rate monitoring," IEEE Trans. Instrum. Meas. **71**, 1–15 (2022).